

# ANALYSIS OF NOTCH STRAINS COMBINING ELECTRONIC SPECKLE PATTERN INTERFEROMETRY AND DIGITAL IMAGE CORRELATION

Thomas LEHMANN\*, Jörn IHLEMANN

*Chemnitz University of Technology, Chair of Solid Mechanics, Chemnitz, Germany*

\*corresponding author, [thomas.lehmann@mb.tu-chemnitz.de](mailto:thomas.lehmann@mb.tu-chemnitz.de)

In this contribution, electronic speckle pattern interferometry (ESPI) and digital image correlation (DIC) are combined for strain analysis around a notch. The investigations are demonstrated using an epoxy notched cantilever bending beam. For the evaluation of the experimental raw data a special method is used, which includes parametrization of the notch surrounding region and optimized smoothing. Thus, the determination of more precise results of the ESPI and DIC analyses is enabled compared to standard evaluation procedures. The deformation measurement methods complement each other profitably, considering the respective limitations and potentials of the ESPI and DIC.

**Keywords:** electronic speckle pattern interferometry; digital image correlation; strain; smoothing.



Articles in JTAM are published under Creative Commons Attribution 4.0 International.  
Unported License <https://creativecommons.org/licenses/by/4.0/deed.en>.  
By submitting an article for publication, the authors consent to the grant of the said license.

## Nomenclature

### Symbols

$a$  – coordinate (general),  
 $B, \bar{B}$  – matrices of the fast Fourier transform,  
 $C$  – correlation coefficient,  
 $c$  – subpixel shift resolution,  
 $d$  – diameter,  
 $f$  – objective function,  
 $I$  – intensity,  
 $k$  – aperture number ( $f$ -number),  
 $l$  – length (width, height), size,  
 $M$  – magnification,  
 $n$  – number of pixels,  
 $R, r$  – radius,  
 $s$  – parameter of the annulus,  
Tol – smoothing parameter (tolerance),  
 $T$  – thickness  
 $t$  – parameter of the annulus,  
 $u$  – displacement,  
 $x, \bar{x}, y, \bar{y}$  – coordinates,  
 $\Delta$  – difference,

### Subscripts/superscripts

$i$  – frame number,  
 $j$  – condition,  
 $ij$  – matrix indices,  
 $m$  – modulated,  
 $p$  – punch,  
res – resulting,  
 $s$  – speckle,  
 $u$  – displacement,  
 $0$  – basic,  
1, 2, 3, ... – condition, frame number.

### Abbreviations

C – camera,  
DG – diffraction grating,  
DIC – digital image correlation,  
EO – expansion optics,  
ESPI – electronic speckle pattern interferometry,  
FFT – fast Fourier transform,  
LS – light source,  
M – mirror,



Ministry of Science and Higher Education  
Republic of Poland

The publication has been funded by the Polish Ministry of Science and Higher Education under the Excellent Science II programme “Support for scientific conferences”.

The content of this article was presented during the 40th Danubia-Adria Symposium on Advances in Experimental Mechanics, Gdańsk, Poland, September 24–27, 2024.

$\varepsilon$ – strain,	O – object,
$\eta$ – error measure,	PO – parallelization optics,
$\theta$ – beam angle,	Pz – piezo actuator,
$\lambda$ – wavelength of the laser,	ROI – region-of-interest,
$\varphi, \phi$ – phase,	S – shutter.
$\psi$ – angle of the annulus.	

## 1. Introduction

The determination of inhomogeneous deformations is of particular importance in experimental mechanics. Examples of such analyses can be found in experimental deformation and stress analyses of structures. Furthermore, it may be required in the verification and validation of simulation models of complex structures with inhomogeneous strain and stress states. Other examples of analyzing inhomogeneous strain fields are the characterization of materials, parameter identification for material models (high information density due to the inhomogeneous strain distribution) and measurements with component-oriented specimens. In order to meet the high requirements of such analyses, powerful field measurement methods are used. In experimental deformation analysis, two measuring methods have become established, which are also particularly suitable for inhomogeneous strains. These are electronic speckle pattern interferometry (ESPI) and digital image correlation (DIC) which operate on completely different physical and mathematical principles and in different measuring ranges (the basics to the methods are given for ESPI in (e.g., [Jacquot, 2008](#); [Dudescu, 2015](#)) and for DIC in (e.g., [Sutton \*et al.\*, 2009](#))). The basis of the ESPI principle is interference of coherent light wave trains with evaluation of the intensity of the speckle pattern formed through interference. In contrast, DIC is based on the correlation of gray value distributions of the surface by a matching algorithm. By both methods 2D and also 3D displacement fields of optically accessible surfaces can be determined. However, the measuring ranges are very different depending on the method. ESPI has an upwardly limited measuring range regarding one-step analysis due to the physical basic principle. However, the precision of this method is very high for small deformations. DIC, on the other hand, can be very well used to measure large deformations, but shows limited precision in the lower deformation range due to the lower sensitivity of the method depending on the respective parameters (setup, conditions, DIC and strain evaluation algorithm). These limitations resulting from the measuring principles cannot or can only hardly be influenced by improving the device technology and the evaluation method. A combination of both measuring methods, in which ESPI is used in the lower deformation range and DIC for larger deformations, would enable an increase in measurement opportunities and precision. In the framework of this paper, the corresponding 2D techniques are used. The analysis of surface contours is not possible by means of these measurement methods. Therefore, e.g., surface topography investigations cannot be carried out in this way. Examples of such analyses can be found in ([Macek \*et al.\*, 2023](#); [Kobayashi & Shockey, 2010](#)).

In ESPI as well as DIC analyses the displacement fields are measured, which can be further processed. On the basis of the displacements, strains can be determined by various methods, which is independent of the measuring method. The frequently used standard strain evaluation method is based on local evaluations using measured coordinates of adjacent points, e.g., for DIC in ([Carl Zeiss GOM, 2016](#)). However, when this standard evaluation method is used, the precision of the analysis will be particularly limited in the respective range of the measuring method. This can be observed for example using standard strain evaluation tools of commercial DIC software. Due to the noisy raw data, smoothing is recommended or can be required. One way is the use of filters such as spatial mean or median filters in the vicinity of a point (see ([Sun & Qu, 2014](#))). Another method is strain calculation based on smoothing of the displacement data using the finite element method (FEM), as a global approach that can be found in (e.g., [Avril \*et al.\*, 2008](#)). A further global approach to calculate strains is based on the approximation

of raw data by functions. For example, polynomials (cf. Kirbach *et al.* (2015), Pierron *et al.* (2007)) or B-splines can be used for this purpose. Basics of B-spline approximation can be found in (Hoschek & Lasser, 1992) and a selection of application examples are given in (Lehmann *et al.*, 2018; 2019; Peretzki *et al.*, 2022; Lehmann & Ihlemann, 2022; Kanzenbach *et al.*, 2022). Using an approximation-based method, strains are easily determined by derivatives and smoothing is achieved by the continuous mathematical description due to the functions (in most cases the displacement). However, using polynomials, overshooting effects at the edges can occur producing significant errors. This can be reduced or at best avoided by using B-splines, which also enables an improved smoothing control, which is shown in (Lehmann *et al.*, 2018). Though, following this approach, errors can occur near sections where no data is available (e.g., notches, holes). In order to avoid these effects, a parameterization of the surrounding region (near these boundaries) can be used to improve the accuracy of the strain evaluation, demonstrated for a notch in (Lehmann *et al.*, 2019). Furthermore, approximation using B-splines may be improved by analyzing the occurring noise, which enables the optimization of the smoothing control parameter shown in (Lehmann & Ihlemann, 2022; Kanzenbach *et al.*, 2022).

In the present paper, both measuring methods – 2D ESPI with phase shifting technique and 2D DIC – are evaluated regarding their resolution and measuring range. A combination of both methods in one setup is presented. The in-plane deformation analysis at a notch is performed by parametrization of the surrounding region and approximation of the raw ESPI and DIC data by B-splines. Furthermore, an optimization of the smoothing is performed considering the characteristic noise properties of the data in the approximation process.

## 2. Preliminary considerations regarding displacement resolution and largest detectable displacement of the measurement methods

### 2.1. 2D ESPI with phase shifting

Using the phase shifting technique in ESPI, the resolution of the basic method is increased. The principle is based on a shift (change) of the phase  $\varphi$  in a speckle pattern due to displacement of points in two loading conditions  $j = 1, 2$  (e.g., unloaded, loaded). The speckle patterns are formed by interference of two laser object beams (coherent light). A precondition is a diffuse reflecting object surface. Considering the resulting intensity  $I_{\text{res}}$  of the speckle pattern, given by:

$$I_{\text{res}}(x, y) = I_0(x, y) + I_m(x, y) \cos \varphi(x, y), \quad (2.1)$$

the phase  $\varphi$  cannot be calculated directly. This is caused by the unknown basic and modulated intensity  $I_0$  and  $I_m$ . Using temporal phase shifting technique, a minimum of 3 additional phase shifts (angles) are necessary for the determination of the phase  $\varphi$ . In order to increase the data base, 4 additional phase shifts are implemented. In the contribution presented, an appropriate 4-frame-algorithm is used with the phase shifts  $0, \frac{\pi}{2}, \pi, \frac{3}{2}\pi$  resulting in 4 different intensities  $I_{\text{res } i}$ . The phase in the two conditions ( $j = 1, 2$ ) is determined by:

$$\varphi_j(x, y) = \arctan \frac{I_{\text{res } 4j}(x, y) - I_{\text{res } 2j}(x, y)}{I_{\text{res } 1j}(x, y) - I_{\text{res } 3j}(x, y)}. \quad (2.2)$$

Finally, the phase difference  $\Delta\varphi(x, y)$  is defined by:

$$\Delta\varphi(x, y) = \varphi_2(x, y) - \varphi_1(x, y). \quad (2.3)$$

These calculations are carried out for the directions  $x$  and  $y$ . Due to the basic equations,  $\Delta\varphi$  is discontinuous ( $\Delta\varphi \in (-\pi, \pi]$ ) with a phase modulo of  $2\pi$ , which results in the respective

phase maps. Thus, unwrapping the distribution  $\Delta\varphi$  is required to obtain the associated continuous phase difference  $\Delta\phi$  used for displacement determination. The displacement fields  $u_a$  with  $a = x, y$  are calculated by:

$$u_a(x, y) = \frac{\lambda}{4\pi \cdot \sin \theta} \cdot \Delta\phi_a(x, y), \quad (2.4)$$

where  $\lambda$  is the wavelength of the laser and  $\theta$  the beam angle of the object beams. Furthermore, the appropriate sign needs to be considered according to the coordinate axis definition. As aforementioned, between the phase edges a phase difference of  $2\pi$  occurs in the phase maps, which is usually represented in the gray value distribution. For an example with the parameters  $\lambda = 532 \text{ nm}$  and  $\theta = 39.67^\circ$  the displacement step using Eq. (2.4) is 417 nm. Using 8 bit resolution for the displayed grey scale distribution, 256 grey values are provided. This leads to a theoretical minimum detectable displacement in  $x$ - and  $y$ -directions of  $\Delta u_{\min a} = 1.6 \text{ nm}$  representing a theoretical resolution of ESPI with phase shifting for this example. In practical analyses, the variance error of a measuring sequence in the same load condition can be considered to determine the noise and thus the approximated practical achievable resolution. It depends, in addition to the determining influencing parameters, on the actual conditions of the respective experimental setup. Hence, the practical minimum detectable displacement values will increase.

For displacement of object points, displacements in the speckle pattern occur in addition to the desired phase shift. The ESPI theory is based only on intensity changes of the speckle. Therefore, in experimental applications of the method it is assumed that the speckles shift and deform only very slightly, which leads to a considerable limitation of the measuring range upwards. This concerns the measurement in one step. The restriction of displacement depends on the speckle size. Experimental experiences show that stable phase maps cannot be calculated, when the displacement (absolute value) exceeds approximately  $0.25 \dots 0.4 \cdot d_s$ . Hereby,  $d_s$  is the approximated speckle diameter. It results from the wavelength as well as the imaging conditions and is determined at the object by the following equation (cf. Rohrbach (1989), Cloud (2007)):

$$d_s \approx 1.2 \lambda k \left( 1 + \frac{1}{M} \right). \quad (2.5)$$

Herein,  $k$  is the aperture number ( $f$ -number) and  $M$  is the magnification given by the optical system. For an example of  $\lambda = 532 \text{ nm}$ ,  $k = 11$ , and  $M = 0.3$  the speckle size  $d_s$  is approximately  $30 \mu\text{m}$ . Thus, for this example, the maximum approximately detectable absolute displacement value in one step at the object is  $\Delta u_{\max} \approx 8 \dots 12 \mu\text{m}$  under the above condition.

## 2.2. 2D DIC

The principle of 2D DIC is based on correlation of grey scale distributions with the consideration of point environment defined by a subset of pixels in the digital images. The coordinates in a second condition (e.g., loaded) are determined using a matching algorithm. As DIC is a well-known and meanwhile frequently used method, the basics are not given in detail here. The principle and examples are well described in the literature (e.g., Sutton *et al.*, 2009).

The minimum detectable displacement  $\Delta u_{\min a}$  as displacement resolution depends strongly (linear dependency) on the subpixel shift resolution  $c$ . Typical values for  $c$  are between 0.1 and 0.25 pixel and depend on the actual experimental conditions influencing the quality of the images acquired and the matching algorithm. For special conditions, values of  $c = 0.01$  pixel even can be reached. The value  $c$  is multiplied by the image scale  $l_a/n_a$  in mm/pixel as it is given by:

$$\Delta u_{\min a} = \frac{l_a}{n_a} c, \quad (2.6)$$

where  $l_a$  is the width or height of the measuring field (field-of-view) and  $n_a$  is the number of pixels at the camera chip in the respective direction. For an example with the image scale  $l_a/n_a = 0.01 \text{ mm/pixel}$  and with an estimated value  $c = 0.1 \text{ pixel}$ , according to Eq. (2.6) the minimum detectable displacement is  $\Delta u_{\min a} = 1 \mu\text{m}$ .

On the other hand, generally large displacements and strains can be measured with DIC. Depending on the calculation options and the algorithm of the DIC system, an approach to limitation in the form of the theoretical maximum detectable displacement in one step can be (approximately):

$$\Delta u_{\max a} \approx l_a - l_{\text{subset}}, \quad (2.7)$$

considering the subset size  $l_{\text{subset}}$  as well as the field-of-view size  $l_a$ . Following this approach, for an example with  $l_x = 24.7 \text{ mm}$  and  $l_{\text{subset}} = 0.25 \text{ mm}$ , a value of  $\Delta u_{\max x} \approx 24.45 \text{ mm}$  is calculated. That is approximately the dimension  $l_x$ .

### 3. Experimental setup and procedure

#### 3.1. Setup

The experimental setup is complex due to the general requirements of the in-plane ESPI method. Additionally, it is extended by the application of DIC. The principle of the setup is given in Fig. 1. Beyond, the real experimental setup is depicted in Figs. 2 and 3.

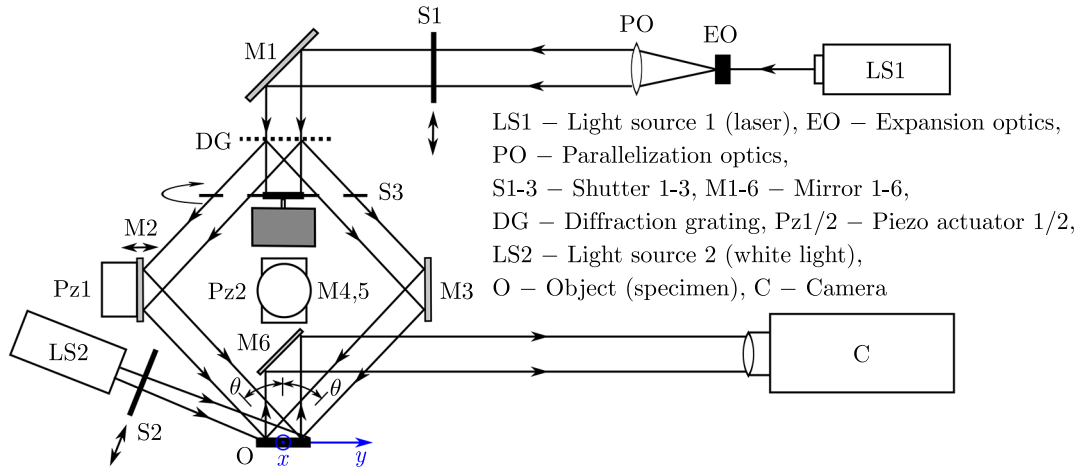


Fig. 1. Principle of the experimental setup including ESPI (based on Lehmann *et al.* (2019)) and DIC equipment.

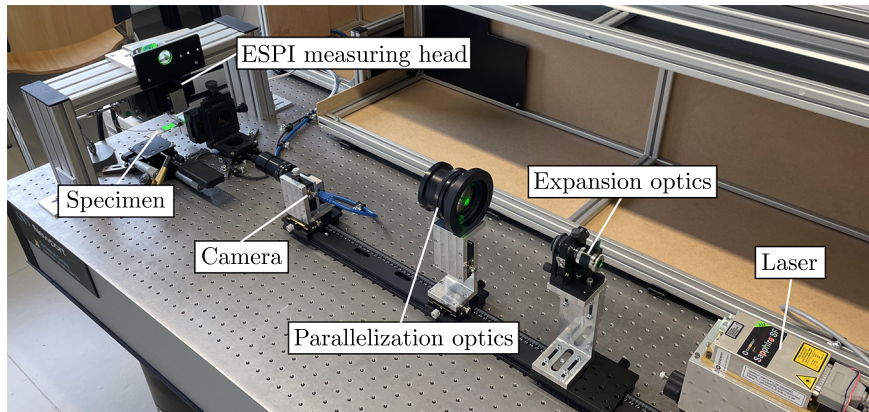


Fig. 2. Real experimental setup including ESPI and DIC equipment.



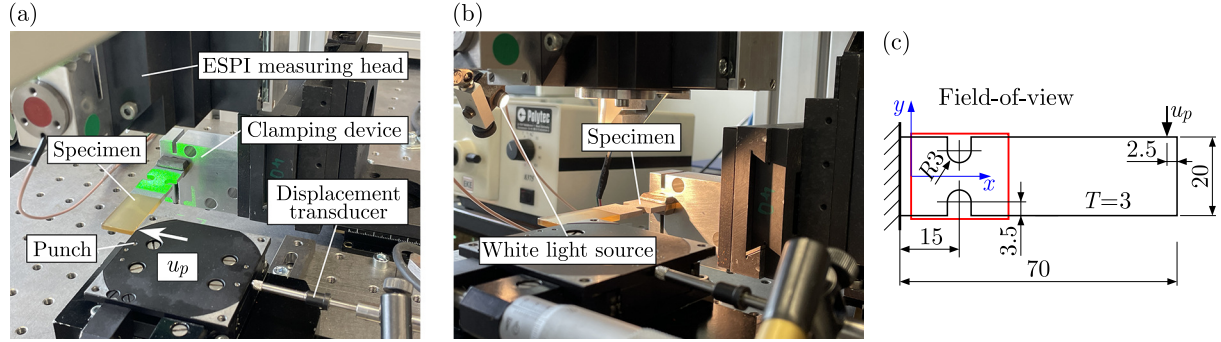


Fig. 3. Details of the experimental setup – specimen and surrounding components: a) during ESPI analysis (green laser light); b) during DIC analysis (white light); c) specimen geometry and load case (based on [Lehmann et al. \(2019\)](#)).

The basis of the setup is a self-developed 2D ESPI device including an optically pumped semiconductor laser from Coherent, of the type Sapphire 532 SF with a wavelength of  $\lambda = 532\text{ nm}$ , LS1. The focused beam is expanded by the expansion optics EO with a pinhole. The next step is the parallelization using the optical paralleling lens PO, which includes an aperture for limitation adjustment of the beam diameter. Then, from horizontal direction, the expanded and parallelized beam is deflected to the vertical direction by reflection at a mirror M1 which is arranged in a  $45^\circ$  angle. The beam is divided by a diffraction grating DG (cross grating for the two directions with 1200 lines per mm), so that the orders  $-1$  and  $1$  are symmetrically guided within the ESPI measuring head (see also [Figs. 2](#) and [3](#)) to further mirrors M2/M3 (for the  $y$ -direction) and M4/M5 (for the  $x$ -direction), respectively. The two beams are reflected and symmetrically radiated to the object O (specimen) under the beam angle  $\theta = 39.67^\circ$ . Finally, the reflected and interfering laser light is reflected by an additional  $45^\circ$  arranged mirror M6 and observed by the camera C (Baumer, type VCXU-50M, CMOS camera with resolution of 5 megapixels). For the temporal phase shifting technique, the additional phase shifts are applied using piezo actuators Pz1 (for the  $y$ -direction) and Pz2 (for the  $x$ -direction). Shutter S3, which can be rotated by a stepper motor, covers the direction not currently being analyzed by the respective angle position. To perform the ESPI analyses, the shutter S2, which blocks the white light source LS2 (cold light source with fiber optic cable, see [Fig. 3b](#)), is closed in order to use only the laser light.

In contrast, the shutter S1 is closed for the DIC analyses in order to block the laser light. Furthermore, the shutter S2 is open enabling illumination of the specimen (object) with white light. The light reflected at the object is then deflected by the mirror M6 to provide the horizontal direction of the light path. Thus, for acquisition of the DIC images, the same camera C is used as in the ESPI measurement.

A notched cantilever bending beam made of epoxy resin is used as the object, see [Figs. 2](#) and [3](#). For the DIC measurement, a fine speckle pattern was produced by coating using black and white spray paint at the surface of the specimen. The properties of the coating are such that a diffusely reflecting surface with corresponding roughness is created, which is also suitable for the ESPI analysis. The specimen is fixed by a clamping device and the bending load is applied by a manually adjustable linear unit acting as a punch (punch displacement  $u_p$  measured by an incremental displacement transducer, Heidenhain MT 25). The specimen geometry and the field-of-view (dimensions  $24.7 \times 20.7$ , width  $\times$  height in mm) observed by the camera are given in [Fig. 3c](#).

### 3.2. Test procedure

The specimen was loaded by punch displacement in steps of  $u_p = 15\text{ }\mu\text{m}$ ,  $30\text{ }\mu\text{m}$ ,  $60\text{ }\mu\text{m}$ , and  $120\text{ }\mu\text{m}$ . In each load step, grey scale images were acquired successively to apply both

methods, ESPI and DIC. A reference state was adjusted with a preload to obtain defined initial conditions and to ensure that the punch is in contact with the specimen. Image acquisition for ESPI (automatically within the phase shifting 4-frame-algorithm with piezo and shutter control) and for the DIC analysis was performed using a self-developed ESPI software. In the reference state, 4 ESPI phase shift images (for both directions  $x$  and  $y$ ) and 1 DIC image were recorded. In the deformed state (relative to the reference state), a set of ESPI images ( $4 \times 4$  images per direction) and 4 DIC images were taken, that is a repetition of image acquisition in the same condition was carried out. These images are used as a basis for the noise analysis and deformation calculation.

For the 2D ESPI measurements with phase shifting, calculations are carried out using the aforementioned self-developed measurement software. The primary results calculated by the software are the phase maps according to Eqs. (2.2) and (2.3). In the following step the raw phase map data is processed using a filter to obtain sharp phase edges and suitable grayscale distributions in the final phase map, which is used for calculation in further steps. For the DIC procedure, the respective images acquired were analyzed by the DIC inspection software GOM Correlate Professional. For the conversion of the data in mm, the image scale was determined and implemented. The DIC correlation algorithm was performed regarding the first image with subset (facet) size of 25 pixels (0.25 mm) and a step size of 20 pixels (0.20 mm). The primary results are the coordinates, which were provided as data for further processing.

#### 4. Evaluation method

The displacement and strain calculation were performed using a post processing procedure in MATLAB for both measurement methods. The individual process steps are presented in the following.

##### 4.1. Determination and processing of displacements

As described in Subsection 2.1, in the ESPI analysis the discontinuities of the phase difference  $\Delta\varphi_a$  must be dissolved by an unwrapping algorithm. The continuous phase difference  $\Delta\phi_a$  is determined in this paper by unwrapping with a procedure implemented in MATLAB, given by Herráez *et al.* (2002) and Kasim (2017). Furthermore, by Eq. (2.4) the ESPI displacement fields  $u_x$  and  $u_y$  are obtained. However, this displacement raw data is noisy to a certain extent, so that the accuracy of further calculations can be improved by smoothing. Regarding DIC, in this contribution, the displacements as raw data were calculated within the post processing procedure based on the coordinates (by difference calculation) in the different loading conditions instead of using the direct software displacement results. Because the DIC data is noisy, smoothing is here required too.

Besides displacement evaluation over the whole field-of-view based on the raw ESPI and DIC data, the surrounding region around the upper notch root is considered as a special region-of-interest (ROI) for further analysis. Due to the characteristic of strain analysis at notch edges described in Section 1, this annulus region is analyzed implementing a parametrization. This approach was first demonstrated in a similar way by the authors and tested for ESPI analyses including comparison with numerical simulation in (Lehmann *et al.*, 2019). To this end, normalized parameters  $s$  and  $t$  considering an angle  $\psi$  are introduced as follows, cf. Fig. 4:

$$\begin{aligned} s(\psi = 0^\circ) &= 0, & s(\psi = 180^\circ) &= 1, \\ t(r = r_{\min}) &= 0, & t(r = r_{\max}) &= 1. \end{aligned} \tag{4.1}$$

In the presented analyses,  $r_{\min}$  is defined at a distance of approximately 0.2 mm from the edge of the notch, as error-influenced raw data occurs directly at this edge. Furthermore, as shown in Fig. 4, in addition to the  $xy$ -coordinate system, local coordinates  $\bar{x}$  and  $\bar{y}$  are used. By the

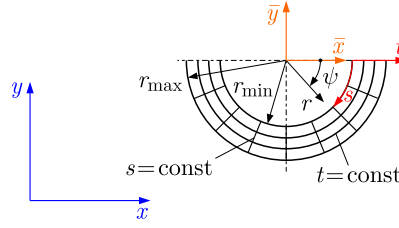


Fig. 4. Parametrization of the notch surrounding region.

parameters  $s$  and  $t$ , which are functions which depend on the coordinates  $\bar{x}$  and  $\bar{y}$ , a dimensionless  $1 \times 1$  square is formed. The relations are based on the geometry and are given by:

$$s(\bar{x}, \bar{y}) = \frac{\arctan(-\bar{y}/\bar{x})}{\pi} \quad \text{and} \quad t(\bar{x}, \bar{y}) = \frac{\sqrt{\bar{x}^2 + \bar{y}^2} - r_{\min}}{r_{\max} - r_{\min}}. \quad (4.2)$$

Hence, in the defined parametrized notch ROI, approximation can be performed with all existing measuring data to obtain the displacement functions  $u_a(s, t)$ .

The approximation of the ESPI and DIC displacements is carried out using cubic B-splines considering characteristic noise properties (referred to as the approximation-based method). Within this algorithm, the smoothing parameter  $\text{Tol}_{u_a}$ , representing a controlling parameter for the displacement approximation, is determined by an optimization procedure. Basics of the optimization method are given by [Lehmann and Ihlemann \(2022\)](#) and [Kanzenbach et al. \(2022\)](#). The principle is depicted in [Fig. 5](#).

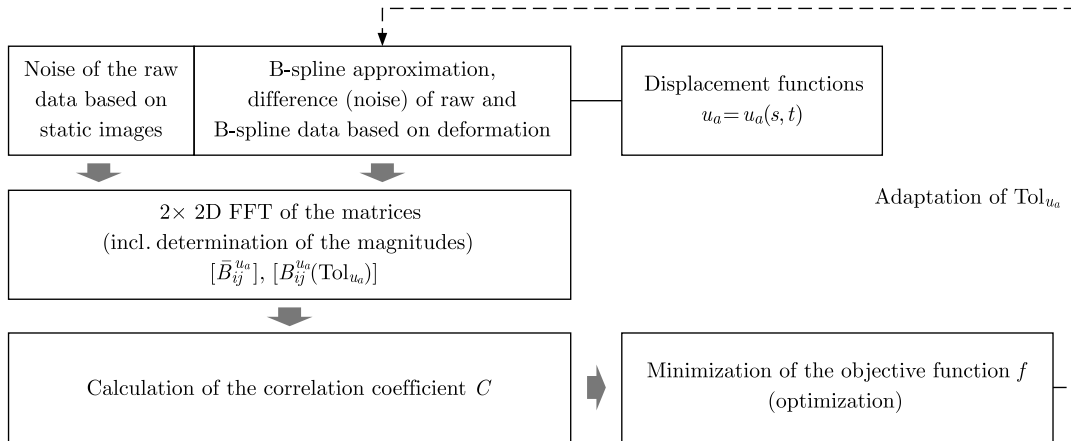


Fig. 5. Displacement approximation with optimized smoothing.

The spatial noise of the raw data is analyzed based on static images, that is in a loading condition without changes of the load and without movement of the specimen. Since the algorithm should also be suitable for ESPI measurements based on characteristic phase maps, the deformed state was selected for this noise analysis of the raw data. Hence, the database is a sequence of resulting static ESPI phase maps or DIC images in the deformed state. The noise of the raw data is defined by the difference between two displacement fields based on the noise images. If necessary, components with significantly lower spatial oscillation (long-wave variation) within the noise database are filtered out by a mean filter additionally. Furthermore, the displacements in the deformed state are analyzed as a difference to the reference state and approximated by B-splines as described. Here, the difference between the raw and B-spline data based on deformation represents the resulting noise. The object of optimizing the smoothing parameter  $\text{Tol}_{u_a}$  is to achieve good correlation of the noise characteristics. For this purpose, a first 2D fast Fourier transform (FFT) of the matrices (field data of the noise analysis) with calculation of the magnitudes is performed. Tests have shown that the noise properties show good correlation



based on optimization, if the FFT is performed twice. Hence, by a second 2D FFT the matrices  $[\overline{B}_{ij}^{u_a}]$  (based on static images) and  $[B_{ij}^{u_a}]$  (based on deformation) are obtained. As a similarity measure of the noise analysis, the Pearson correlation coefficient  $C$  (cf. [Profillidis and Botzoris \(2019\)](#)) is calculated and used for the optimization. Finally, suitable tolerances  $\text{Tol}_{u_a}$  are found by an optimization using the Nelder–Mead simplex algorithm with minimization of the objective function  $f$ :

$$\min_{\text{Tol}_{u_a}} f(\text{Tol}_{u_a}) = \min_{\text{Tol}_{u_a}} \left( 1 - C \left( [\overline{B}_{ij}^{u_a}], [B_{ij}^{u_a}(\text{Tol}_{u_a})] \right) \right). \quad (4.3)$$

## 4.2. Calculation of strains

The strains are determined based on the functions  $u_a(s, t)$ . This requires the partial derivatives of the displacements with respect to the parameters and the partial derivatives of the parameters (based on [Eqs. \(4.2\)](#)) with respect to the coordinates. As an example, the strain  $\varepsilon_x$ , relevant for the investigations demonstrated, is defined by:

$$\varepsilon_x = \frac{\partial u_x}{\partial x} = \frac{\partial u_x}{\partial \bar{x}} = \frac{\partial u_x}{\partial s} \frac{\partial s}{\partial \bar{x}} + \frac{\partial u_x}{\partial t} \frac{\partial t}{\partial \bar{x}}. \quad (4.4)$$

## 5. Results

The results presented are limited to the evaluation of the  $x$ -direction, as the deformation analysis for this load case is relevant in this direction. The evaluation is performed using the procedures described in [Section 4](#).

### 5.1. Phase maps and displacements

For the ESPI analyses, at first the wrapped phase maps are assessed, as these already provide an indication of the quality of the measurement. The load steps with punch displacement  $u_p = 15 \mu\text{m}$  (cf. [Fig. 6a](#)) and  $30 \mu\text{m}$  (cf. [Fig. 7a](#)) show plausible phase differences  $\Delta\varphi_x$  (inclu-

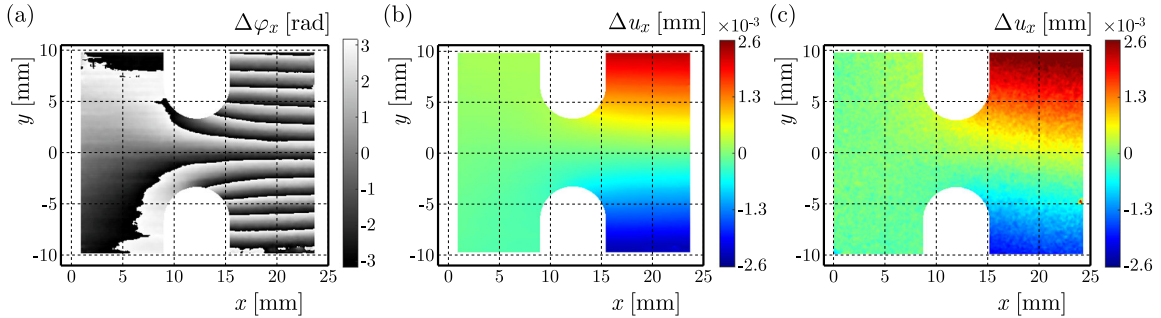


Fig. 6. (a) Phase map  $\Delta\varphi_x$ ; (b) ESPI displacement field  $\Delta u_x$ ; (c) DIC displacement field  $\Delta u_x$  – for punch displacement  $15 \mu\text{m}$ .

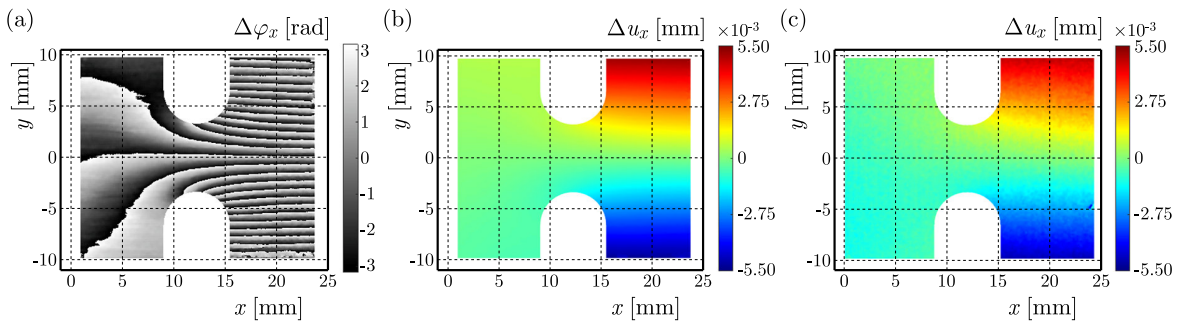


Fig. 7. (a) Phase map  $\Delta\varphi_x$ ; (b) ESPI displacement field  $\Delta u_x$ ; (c) DIC displacement field  $\Delta u_x$  – for punch displacement  $30 \mu\text{m}$ .

ding the discontinuities) with the typical distribution of this load case considering the notched cantilever bending beam.

In the case of the higher load steps of  $u_p = 60 \mu\text{m}$  (cf. Fig. 8a) and  $120 \mu\text{m}$  (cf. Fig. 9a), the limitation of the algorithm takes effect, as the displacements of the speckles are too large and exceed the critical value. This is for  $u_p = 60 \mu\text{m}$  in the region on the right side of the notches (over the full specimen height) and for  $u_p = 120 \mu\text{m}$  approximately in the right half of the field-of-view. By unwrapping, the ESPI displacement fields  $\Delta u_x$  for the lower load steps are obtained, cf. Figs. 6b and 7b. This is expressed as displacement difference regarding the point at the left boundary at  $y = 0$  (at this point the displacement is defined as zero). This approach is the same for the DIC displacements, cf. Figs. 6c, 7c, 8b, and 9b. The ESPI results show an almost symmetrical displacement distribution for the evaluable load steps and the DIC results for the load steps except  $u_p = 15 \mu\text{m}$ . Thus, for  $u_p = 30 \mu\text{m}$  the distributions of ESPI and DIC measurement show good agreement. In the lower load levels (see Figs. 6c and 7c) significantly more noise is observed in the DIC data due to the limited sensitivity of the method.

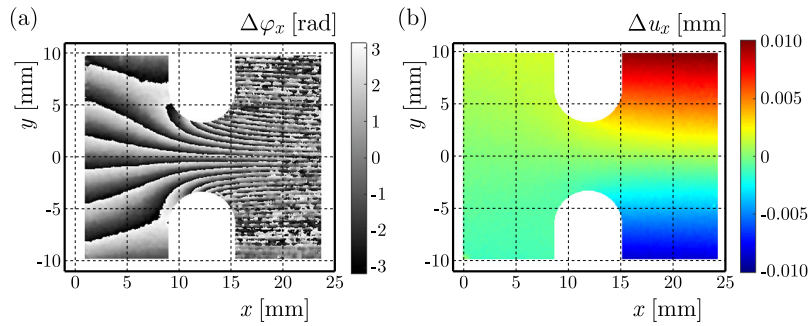


Fig. 8. (a) Phase map  $\Delta\varphi_x$ ; (b) DIC displacement field  $\Delta u_x$  – for punch displacement  $60 \mu\text{m}$ .

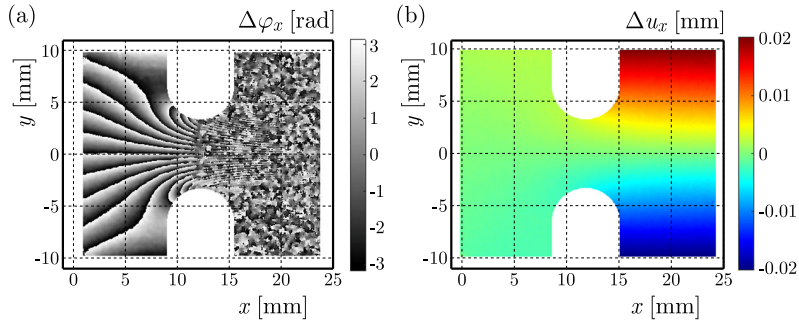


Fig. 9. (a) Phase map  $\Delta\varphi_x$ ; (b) DIC displacement field  $\Delta u_x$  – for punch displacement  $120 \mu\text{m}$ .

The special ROI is the annulus region surrounding the upper notch root, which is parametrized according to the described evaluation method. In Fig. 10, a representative example of the noise analysis, showing the database of  $u_p = 30 \mu\text{m}$ , is given. The noise  $\Delta u_x$  based on static images (analyzed by an image sequence in the deformed state without change of loading), cf. Figs. 10a and 10c, generally show small values, but with different characteristic of the noise distribution for the ESPI and DIC methods. In this example, the noise floor – defined as the spatial standard deviation – is  $1.2 \cdot 10^{-2} \mu\text{m}$  for ESPI and  $6.8 \cdot 10^{-2} \mu\text{m}$  for DIC. The higher precision of the ESPI method is clearly obvious. Furthermore, a small offset value is observed in the noise plot, which indicates that small displayed rigid body shifts occur due to error influences. The comparison with the resulting noise based on deformation (as difference of the raw data and the B-spline approximation) with optimized smoothing (cf. Figs. 10b and 10d) shows good agreement regarding the criterion. Due to the optimization of the smoothing parameter  $\text{Tol}_{u_a}$ , the noise characteristic is appropriately similar.

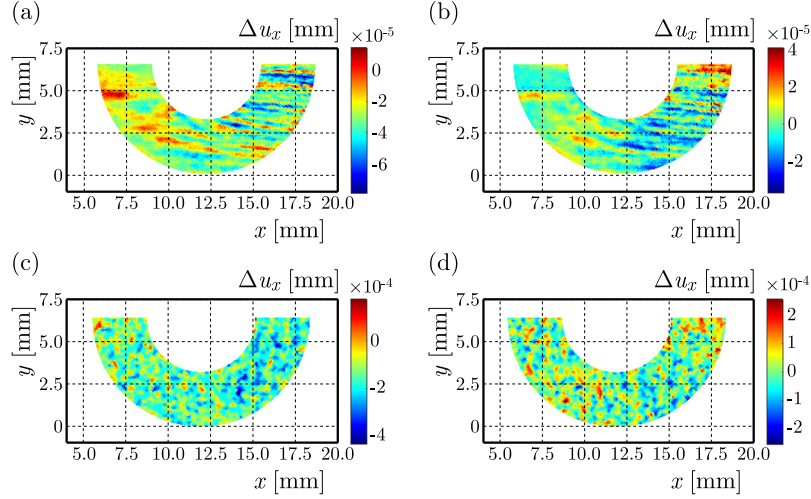


Fig. 10. Comparison of noise distribution  $\Delta u_x$  in the deformed state: (a) ESPI deviation based on static images; (b) ESPI deviation based on deformation; (c) DIC deviation based on static images; (d) DIC deviation based on deformation – for punch displacement  $30 \mu\text{m}$ .

## 5.2. Strains

The strains are based on the parametrization of the notch root surrounding region and approximation of displacements providing suitable functions. All the described extensive evaluations essentially serve the purpose of strain analysis. The strain  $\varepsilon_x$  is finally obtained by calculation using Eq. (4.4). In Fig. 11 the ESPI and DIC strains are compared for the lowest load step with  $u_p = 15 \mu\text{m}$ . Here, significant differences between the results of the methods occur. The ESPI strain shows a more plausible and precise distribution with typical gradients at the notch root.

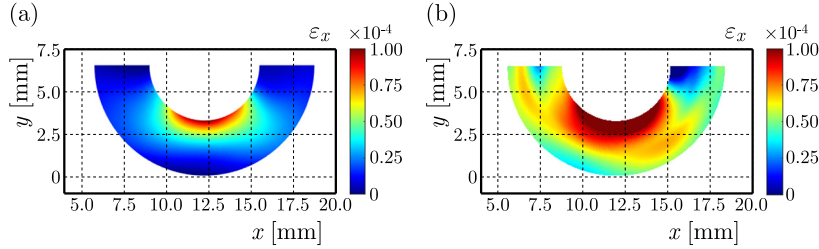


Fig. 11. Strain field  $\varepsilon_x$ : (a) ESPI result; (b) DIC result – for punch displacement  $15 \mu\text{m}$ .

Figure 12 shows good correlation between the strains results of the two measurement methods in the load step with  $u_p = 30 \mu\text{m}$ . For a better quantitative evaluation of the deviations, an error measure  $\eta_x$  is introduced:

$$\eta_x = \frac{\varepsilon_x^{\text{DIC}} - \varepsilon_x^{\text{ESPI}}}{|\varepsilon_x^{\text{ESPI}}|_{\max}}. \quad (5.1)$$

Therein, strain differences regarding the maximum absolute value of the ESPI strain  $|\varepsilon_x^{\text{ESPI}}|_{\max}$  are considered, where  $\varepsilon_x^{\text{DIC}}$  and  $\varepsilon_x^{\text{ESPI}}$  are the strains obtained by the respective methods. The largest deviations occur in the left region of the ROI (annulus). The more precise result is represented by the ESPI strain due to the higher sensitivity, which leads to good suitability of the method for measuring these small strains. It should be noted that this deviation evaluation is one example. Generally, small deviations between the measurements performed at different times at the same load occur for both methods (based on the image sequence in the deformed state). Since the loading was not changed during the step, this is due to errors in the test setup and conditions.

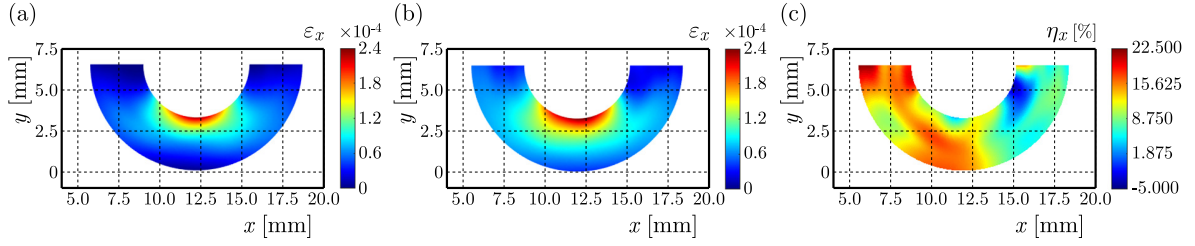


Fig. 12. (a) ESPI strain field  $\varepsilon_x$ ; (b) DIC strain field  $\varepsilon_x$ ; (c) local error measure field  $\eta_x$  (relative deviation between DIC and ESPI) – for punch displacement  $30\ \mu\text{m}$ .

At the higher load steps, the strain cannot be determined by the ESPI method, as the displacements are too large for the algorithm (cf. Figs. 8a and 9a). The DIC strains of the higher load steps are determined by the described approximation-based method with parametrization and additionally by the standard method (without filter), which is provided by the DIC software GOM Correlate Professional and are depicted in Fig. 13 (for  $u_p = 60\ \mu\text{m}$ ) and Fig. 14 (for  $u_p = 120\ \mu\text{m}$ ). The approximation-based method with parametrization (cf. Figs. 13a and 14a) shows more precise results of the strain distribution compared to the standard method (cf. Figs. 13b and 14b). The reason can be found in the basically noisy raw data. It influences the local approach used in the standard method resulting in visible noise of the strain. Smoothing could be achieved by a filter, but with occurring bias at the edges. The higher the strain, the more precise the standard method becomes.

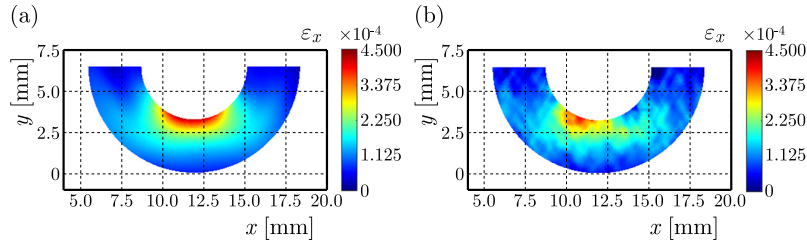


Fig. 13. (a) DIC strain field  $\varepsilon_x$  using the approximation-based method with parametrization; (b) DIC strain field  $\varepsilon_x$  using the standard method – for punch displacement  $60\ \mu\text{m}$ .

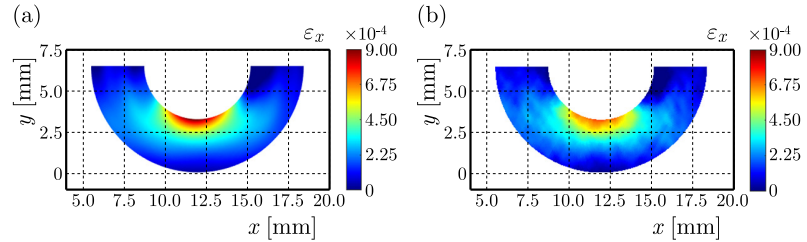


Fig. 14. (a) DIC strain field  $\varepsilon_x$  using the approximation-based method with parametrization; (b) DIC strain field  $\varepsilon_x$  using the standard method – for punch displacement  $120\ \mu\text{m}$ .

## 6. Conclusions

In this paper, a test setup for deformation analysis combining ESPI and DIC is introduced. The setup enables the measurement of displacement fields with both methods in the same load step. This is demonstrated by a bending load case using an epoxy notched cantilever bending beam. The combined ESPI and DIC measurements were successfully performed for different loads. Regarding the basic displacement determination, the following can be concluded:

- The higher sensitivity of the ESPI method leads to more precise results of the displacements demonstrated at the lower load steps (punch displacement  $u_p = 15\ \mu\text{m}$  and  $30\ \mu\text{m}$ ) compared to DIC. Nevertheless, due to the occurring noise floor ( $1.2 \cdot 10^{-2}\ \mu\text{m}$  for an

evaluation example), the theoretical displacement resolution of ESPI described in Subsection 2.1 cannot be reached. Furthermore, the fundamental limitations regarding sensitivity of DIC were confirmed. However, the short-wave characteristic noise of the DIC displacements shows good results (noise floor of  $6.8 \cdot 10^{-2} \mu\text{m}$  for an evaluation example) providing a positive impact on the resolution.

- At the higher load steps large regions – that is the region on the right side of the notches for  $u_p = 60 \mu\text{m}$  and the right half of the field-of-view for  $u_p = 120 \mu\text{m}$  – cannot be analyzed by ESPI due to too large displacements of the speckles. Hence, the limitation of the applicability of ESPI regarding increasing displacements was demonstrated. In contrast, the results confirm that the DIC method is well applicable with larger displacements.

Furthermore, strain evaluation was carried out, which is concluded as follows:

- A special approximation-based evaluation method considering characteristic noise properties with parametrization of the notch root surroundings (developed by the authors) was adapted and advantageously applied. For both measurement methods, the characteristic spatial noise of the raw data based on static images in the deformed state was used as the basis for the optimized smoothing. In that way, good correlation of the resulting noise based on deformation with the noise based on static images is provided. The obtained functions are used for strain determination.
- In the smallest load step ( $u_p = 15 \mu\text{m}$ , maximum strain  $\varepsilon_x \approx 1 \cdot 10^{-4}$ ) the precision of the DIC is not sufficient. In contrast, ESPI provides precise results with plausible distribution due to the high sensitivity of the method. In the load step with  $u_p = 30 \mu\text{m}$  (maximum strain  $\varepsilon_x \approx 2.4 \cdot 10^{-4}$ ) the results of both methods show good correlation of the strain. Here too, the precision of the ESPI result can be classified as higher.
- Due to the limitations of ESPI mentioned before, strain analysis at the higher load steps could not be performed. However, the DIC shows very plausible and precise results for  $u_p = 60 \mu\text{m}$  and  $120 \mu\text{m}$  (maximum strains  $\varepsilon_x \approx 4.5 \cdot 10^{-4}$  and  $9 \cdot 10^{-4}$ ). Compared to standard evaluation, the approximation-based method with parametrization shows more precision in the results.

Finally, we can conclude that based on the experiments presented, the ESPI and DIC methods complement each other very well in one test setup and enable the extension of the deformation measuring range. Generally, the evaluation method demonstrated in this contribution provides advantages resulting in more precision of the deformation analysis compared to other algorithms, independent of the measuring method used (ESPI or DIC). The possibility of extending the DIC measuring range to smaller strains using the special evaluation method is particularly noteworthy. Occurring influences, which have an impact on the variance on the displacements and strains over time, especially with the used test setup, must be analyzed in future investigations to improve the results. This will also improve the comparison of both measurement methods.

## References

1. Avril, S., Feissel, P., Pierron, F., & Villon, P. (2008). Estimation of the strain field from full-field displacement noisy data. *European Journal of Computational Mechanics*, 17(5–7), 857–868. <https://doi.org/10.3166/remn.17.857-868>
2. Carl Zeiss GOM (Gesellschaft für Optische Messtechnik) Metrology GmbH (2016). *Aramis tutorial: DIC strain computation basics*.
3. Cloud, G. (2007). Optical methods in experimental mechanics, Part 27: Speckle size estimates. *Experimental Techniques*, 31(3), 19–22. <https://doi.org/10.1111/j.1747-1567.2007.00201.x>
4. Dulescu, M.C. (2015). *Optical methods in experimental mechanics of solids* [Habilitation thesis, The Technical University of Cluj-Napoca], Cluj-Napoca, Romania. [https://www.utcluj.ro/media/documents/2015/Habilitation.Thesis.-\\_Dulescu.Cristian.pdf](https://www.utcluj.ro/media/documents/2015/Habilitation.Thesis.-_Dulescu.Cristian.pdf)



5. Herráez, M.A., Burton, D.R., Lalor, M.J., & Gdeisat, M.A. (2002). Fast two-dimensional phase-unwrapping algorithm based on sorting by reliability following a noncontinuous path. *Applied Optics*, 41(35), 7437–7444. <https://doi.org/10.1364/AO.41.007437>
6. Hoschek, J., & Lasser, D. (1992). *Fundamentals of geometric data processing* (in German). Teubner. <https://doi.org/10.1007/978-3-322-89829-6>
7. Jacquot, P. (2008). Speckle interferometry: A review of the principal methods in use for experimental mechanics applications. *Strain*, 44(1), 57–69. <https://doi.org/10.1111/j.1475-1305.2008.00372.x>
8. Kanzenbach, L., Lehmann, T., & Ihlemann, J. (2022). Digital image correlation based characterization of rubber material at large shear deformations in an extended temperature range. *GAMM-Mitteilungen*, 45(3–4), Article e202200009. <https://doi.org/10.1002/gamm.202200009>
9. Kasim, M.F. (2017). Fast 2D phase unwrapping implementation in MATLAB. <https://github.com/mfkasim91/unwrap-phase/>
10. Kirbach, C., Lehmann, T., Stockmann, M., & Ihlemann, J. (2015). Digital image correlation used for experimental investigations of Al/Mg compounds. *Strain*, 51(3), 223–234. <https://doi.org/10.1111/str.12135>
11. Kobayashi, T., & Shockey, D.A. (2010). Fracture surface topography analysis (FRASTA)—Development, accomplishments, and future applications. *Engineering Fracture Mechanics*, 77(12), 2370–2384. <https://doi.org/10.1016/j.engfracmech.2010.05.016>
12. Lehmann, T., & Ihlemann, J. (2022). DIC deformation analysis using B-spline smoothing with consideration of characteristic noise properties. *Materials Today: Proceedings*, 62(Part 5), 2549–2553. <https://doi.org/10.1016/j.matpr.2022.03.368>
13. Lehmann, T., Müller, J., & Ihlemann, J. (2018). DIC deformation analyses of Mg specimens at elevated temperatures. *Materials Today: Proceedings*, 5(13, Part 2), 26778–26783. <https://doi.org/10.1016/j.matpr.2018.08.151>
14. Lehmann, T., Stockmann, M., & Ihlemann, J. (2019). A method for strain analyses of surfaces with curved boundaries based on measured displacement fields. *Materials Today: Proceedings*, 12(Part 2), 200–206. <https://doi.org/10.1016/j.matpr.2019.03.114>
15. Macek, W., Branco, R., Podulka, P., Kopec, M., Zhu, S.-P., & Costa, J.D. (2023). A brief note on entire fracture surface topography parameters for 18Ni300 maraging steel produced by LB-PBF after LCF. *Engineering Failure Analysis*, 153, Article 107541. <https://doi.org/10.1016/j.engfailanal.2023.107541>
16. Peretzki, E., Lehmann, T., & Ihlemann, J. (2022). Adaption of the hole drilling method for residual stress analysis inside plastic parts. *Materials Today: Proceedings*, 62(Part 5), 2523–2527. <https://doi.org/10.1016/j.matpr.2022.03.114>
17. Pierron, F., Green, B., & Wisnom, M.R. (2007). Full-field assessment of the damage process of laminated composite open-hole tensile specimens. Part I: Methodology. *Composites Part A: Applied Science and Manufacturing*, 38(11), 2307–2320. <https://doi.org/10.1016/j.compositesa.2007.01.010>
18. Profillidis, V.A., & Botzoris, G.N. (2019). Chapter 5 – Statistical methods for transport demand modeling. In *Modeling of transport demand* (pp. 163–224). Elsevier Inc. <https://doi.org/10.1016/B978-0-12-811513-8.00005-4>
19. Rohrbach, C. (1989). *Handbook for experimental stress analysis* (in German). Springer. <https://doi.org/10.1007/978-3-642-48659-3>
20. Sun, X.X., & Qu, W. (2014). Comparison between mean filter and median filter algorithm in image denoising field. *Applied Mechanics and Materials*, 644–650, 4112–4116. <https://doi.org/10.4028/www.scientific.net/AMM.644-650.4112>
21. Sutton, M.A., Orteu, J.J., & Schreier, H.W. (2009). *Image correlation for shape, motion and deformation measurements*. Springer. <https://doi.org/10.1007/978-0-387-78747-3>